Stripe antiferromagnetic ground state of the ideal triangular lattice compound $KErSe_2$

Jie Xing,[1,*] Keith M. Taddei,[2,*] Liurukara D. Sanjeewa,[1,*] Randy S. Fishman,[1] Marcus Daum,[3] Martin Mourigal,[3] C. dela Cruz,[2] and Athena S. Sefat[1]

[1]*Materials Science and Technology Division, Oak Ridge National Laboratory, Oak Ridge, Tennessee 37831, USA*
[2]*Neutron Scattering Division, Oak Ridge National Laboratory, Oak Ridge, Tennessee 37831, USA*
[3]*School of Physics, Georgia Institute of Technology, Atlanta, Georgia 30332, USA*

(Received 1 June 2020; revised 22 March 2021; accepted 22 March 2021; published 9 April 2021)

Rare-earth triangular lattice materials have been proposed as a good platform for the investigation of frustrated magnetic ground states. $KErSe_2$, with the delafossite structure, contains perfect two-dimensional Er^{3+} triangular layers separated by potassium ions, realizing this ideal configuration and inviting study. Here we investigate the magnetism of $KErSe_2$ at millikelvin temperatures by heat capacity and neutron powder diffraction. Heat capacity results reveal a magnetic transition at 0.2 K in zero applied field. This long-range order is suppressed by an applied magnetic field of 0.5 T below 0.08 K. Neutron powder diffraction suggests that the zero-field magnetic structure orders with $k = (\frac{1}{2}, 0, \frac{1}{2})$ in a stripe spin structure. Unexpectedly, Er is found to have a reduced moment of $3.06(1)\mu_B$/Er in the ordered state, and diffuse magnetic scattering, which originates at higher temperatures, is found to persist in the ordered state, potentially indicating magnetic fluctuations. Neutron diffraction collected under an applied field shows a metamagnetic transition at ~0.5 T to ferromagnetic order with $k = (0, 0, 0)$ and two possible structures, which are likely dependent on the applied field direction. The zero-field stripe spin structure can be explained by the anisotropic interactions or the first-, second-, and third-neighbor couplings in the antiferromagnetic triangular lattice.

DOI: 10.1103/PhysRevB.103.144413

I. INTRODUCTION

The investigation of geometrically frustrated magnetism is intriguing due to the large ground state degeneracy it can engender [1,2]. Different arrangements of lattices and interaction types can give rise to a wide range of magnetic behaviors, such as long-range antiferromagnetic ordering, spin-liquid physics, spin-glass states, and multicritical phenomena in which small perturbations in magnetic interactions or lattice symmetry have an impact on the realized state [3]. In particular, quantum magnetic states, such as quantum-spin liquids (QSLs), are especially interesting for their novel physics that may ostensibly open a new paradigm in computing. The QSL state generally requires an effective spin $S = 1/2$ in frustrated (triangular) lattices. Such a configuration can manifest large spin fluctuations in the absence of long-range magnetic order (even down to 0 K) and potentially lead to long-range entangled states whose excitations can exhibit non-Abelian statistics [4–6].

Due to their possible Kramers doublets and spin-orbital coupling, rare-earth compounds with odd $4f$ electrons can be treated as $S_{\text{eff}} = 1/2$ at low temperatures and so are a potential avenue to realize QSL physics. For example, the triangular lattice compound $YbMgGaO_4$ has been proposed as having a QSL ground state [7–14]. However, more recently, the intrinsic Mg/Ga disorder was found to perturb the system to other less exotic magnetic states, so a suitable candidate material (preferably less prone to disorder) is still needed [7,11,12,15–18].

The delafossite structure ARQ_2 (A=Li, Na, K, Rb, Cs, Tl, Ag, Cu; R=rare earth or $3/4d$ transition metal; Q=O, S, Se, Te) contains a perfect triangular R site layered sublattice separated by spacer A site ions. This structure and a receptiveness to magnetic ions makes it an ideal framework to search for quantum magnetism. One especially useful feature of the delafossite structure is that the intralayer and interlayer distances between magnetic ions can be tuned by using different spacer ions, potentially allowing for multiple magnetic ground states by changing the R site ion or tuning three-dimensional and two-dimensional interactions. Thus far, promising results have been found in $3d$ transition metal variants of the delafossite structure, which have had considerable interest, with some hints of exotic physics [19–25]. For example, $CuFeO_2$ can stabilize collinear commensurate, noncollinear incommensurate, and collinear incommensurate magnetic structures alternatively via varying the strength of an applied magnetic field from 0 to 15 T [19,26].

When the magnetic ions are rare earths, the lattice is expanded due to the large radius, and the interlayer/intralayer distances are increased, causing further variability in the structure. For instance, $CsRSe_2$ can crystallize in one of two different space groups, $R\bar{3}m$ or $P6_3/mmc$, depending on the rare-earth ion, with both showing perfect rare-earth triangular lattices [27]. In the $AYbSe_2$ family, Yb^{3+} hosts $S_{\text{eff}} = 1/2$ and shows no long-range magnetic order down to the lowest measurement temperature, which may relate to the QSL ground state [28–32]. Furthermore, magnetization measure-

*These authors contributed equally to this work.

ments on single crystals of AYbSe$_2$ revealed several nearby long-range ordered states achievable by applying a magnetic field along different crystallographic directions [29,33–36]. On the other hand, in Ce-based compounds, KCeS$_2$ and CsCeSe$_2$ exhibit the Ce^{3+} $4f^1$ electron configuration, and a long-range order magnetic ground state was found in KCeS$_2$ at ∼0.38 K [27,37]. In addition to these compounds, a spin-glass state was proposed in CsDySe$_2$ based on the AC magnetization measurement [27].

Besides the Ce/Yb materials, Er-based compounds are also attractive in the search for quantum magnetism, and several compounds have already been discovered which seem promising. In ErMgGaO$_4$ there have been several reports of a possible QSL ground state with no apparent long-range order down to the lowest measured temperature [38,39]. Similarly, NaErSe$_2$, KErSe$_2$, and CsErSe$_2$ all exhibit easy-plane magnetic anisotropy with no long-range magnetic order or spin freezing in heat capacity and magnetization measurements down to 0.42 K [27,40,41]. The negative Curie-Weiss temperature $\theta_{CW} \sim 4$ K in KErSe$_2$ indicates the antiferromagnetic interaction between Er^{3+} ions. Interestingly, despite exhibiting no long-range order, both NaErSe$_2$ and KErSe$_2$ were found to exhibit metamagnetic transitions under small magnetic fields when applied in the *ab* plane [40]. Follow-up inelastic neutron scattering work studying the crystal electric field levels of KErSe$_2$ indicated the possibility of large anisotropic spin with low spin along the *c* axis [41,42]. Such results together with the success of the similar Er triangular lattice material ErMgGaO$_4$ demand neutron diffraction measurements to study the magnetic properties down to millikelvin temperatures in KErSe$_2$.

In this paper, we report heat capacity and neutron diffraction measurements performed at ultralow temperatures and under applied magnetic fields on KErSe$_2$ together with first-principles calculations to elucidate its magnetic behavior. Our heat capacity measurements show long-range magnetic order with an onset temperature of ∼0.2 K in zero field. Field-dependent measurements show that the magnetic transition is suppressed with increasing field to below 0.08 K at 0.5 T. Additionally, at higher fields we observe a Schottky peak. Neutron powder diffraction measurements performed at 45 mK indicate a stripe-type magnetic structure at 0 T with ordering vector $k = (\frac{1}{2}, 0, \frac{1}{2})$, a rare order for these systems. Under an applied magnetic field, the stripe-type order is found to be suppressed, leading to a metamagnetic transition at ∼0.5 T to a ferromagnetic $k = (0, 0, 0)$ state. First-principles calculations confirm that this magnetic state is possible in KErSe$_2$ but requires the inclusion of second- and third-nearest-neighbor couplings, placing KErSe$_2$ in a unique region of the delafossite structure exchange interaction phase diagram.

II. MATERIALS AND METHODS

The powder and single-crystal samples of KErSe$_2$ were synthesized by the previously reported method [40]. The single-crystal sample was used for heat capacity measurements, and the powder sample was used for x-ray and neutron diffraction. Phase purity was checked with powder x-ray diffraction, which found only the pure phase of KErSe$_2$ without any impurity peaks. The energy dispersive spectroscopy analysis shows the element molar ratio K:Er:Se is the expected stoichiometric ratio 1:1:2 within error. Temperature-dependent heat capacity was measured in a Quantum Design physical properties measurement system using the relaxation technique.

Neutron powder diffraction measurements were performed on the HB-2A (POWDER) diffractometer of Oak Ridge National Laboratory's High Flux Isotope Reactor [43]. Diffraction patterns were collected using the open-21′-12′ collimator settings (for premonochromator, presample, and predetector collimations, respectively) and the longer-wavelength (2.41 Å) incident wavelength setting. To achieve the desired temperature ranges and measure under an applied magnetic field an Oxford dilution refrigerator insert was used with a cryomagnet allowing a temperature range of 0.03 to 300 K and applied fields between 0 and 5 T. Powder patterns were collected with count times of 4 h per scan. "Order-parameter" scans of peak intensities were collected by centering an individual detector on a peak position and collecting intensity on increasing temperature or applied field.

To ensure the sample achieved the desired millikelvin base temperatures, a custom-built "overpressurizable" sample can was used. To start, 3 g of KErSe$_2$ were pressed into a series of ∼0.5-g pellets and then rolled in Cu foil, thus preventing gain reorientation under the applied magnetic field. The foil-sample assembly was then loaded into a custom-designed Cu powder can which included a small inlet in the lid to allow for pressurization after loading. The lid was sealed using In wire, and the can was then connected to a pressure loader and pressurized with 10 atm of He gas. At 10 atm, the Cu tubing inlet (which was preloaded with In wire) was pressed closed in a hydraulic press and carefully cut. To ensure the 10 atm of He remained in the sample can, He leak checks were performed at each step of the loading process and again 24 h after the can was sealed. Furthermore, as a check on the sample thermometry, powder patterns were collected continuously on cooling such that any nascent magnetic peaks could be monitored. Base temperature runs were not collected until the magnetic peak intensities remained constant for 4 h, ostensibly indicating base temperature was reached or that the moment had saturated.

Analysis of the diffraction data was performed using the Rietveld method as implemented in the FULLPROF software suite [44]. The Thompson-Cox-Hasting psuedo-Voigt peak shape with axial divergence asymmetry was used to fit the instrumental profile of HB-2A [45]. The magnetic structure analysis and solution were performed using the Simulated Annealing and Representational Analysis (SARAH) software [46]. Visualization of the crystal structure was performed using VESTA [47].

III. RESULTS AND DISCUSSION

A. Heat capacity

Figure 1 shows the temperature dependence of the heat capacity of KErSe$_2$ from 1 to 0.08 K. Above 0.4 K, no long-range order is found in the previous report up to 9 T [40]. At zero field, an apparent λ-shaped anomaly was found at

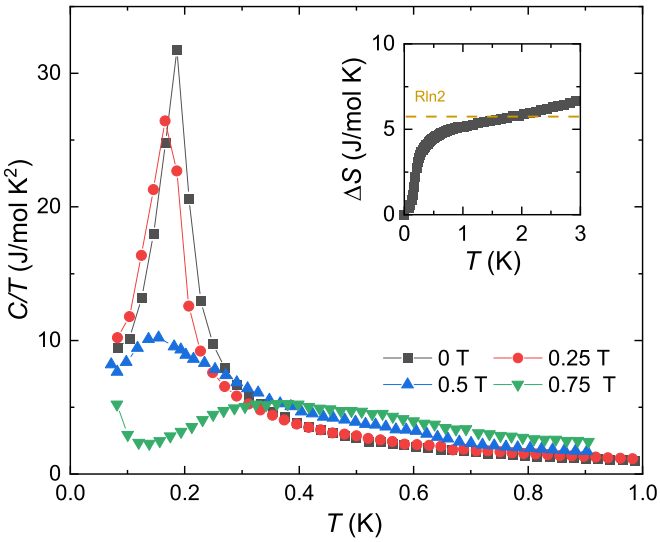

FIG. 1. Temperature dependence of heat capacity from 1 to 0.08 K under different magnetic fields. Inset: Temperature dependence of entropy at 0 T.

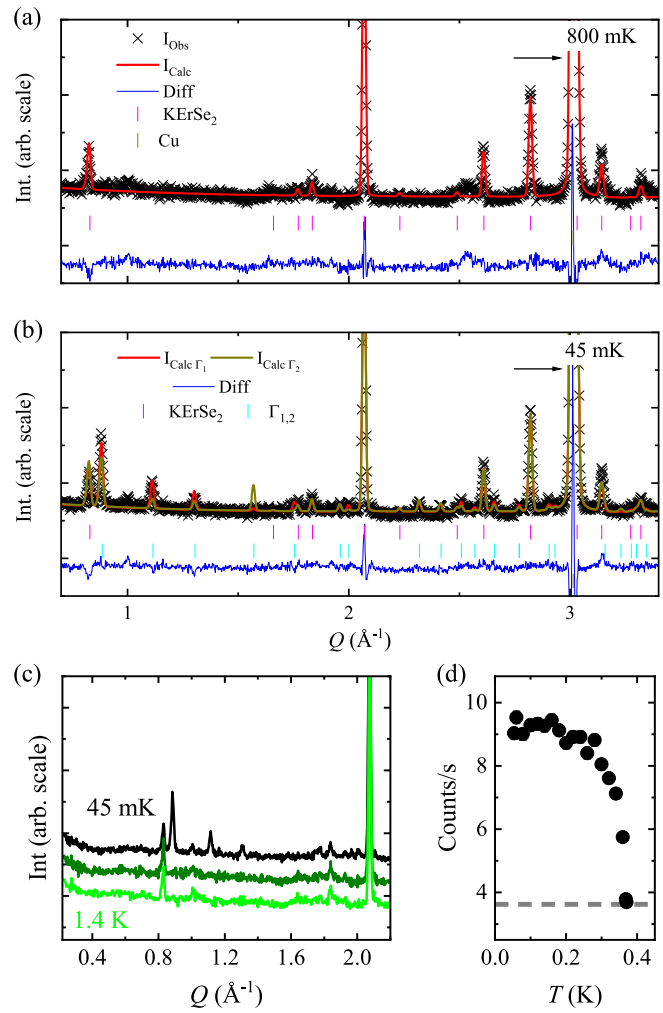

FIG. 2. Neutron powder diffraction data, together with best-fit models determined from Rietveld refinements for data collected at (a) 800 mK and (b) 45 mK. In both panels the data, model, difference, and phase peak indexes are indicated by black crosses, red lines, blue lines, and magenta tick marks, respectively. Indicated by brown tick marks and asterisks are peaks belonging to the Cu sample can. In (b) the cyan tick marks indicate peaks belonging to the magnetic phase generated by the Γ_1 irreducible representation. (c) Neutron diffraction patterns collected at 1.4 K and 800 and 45 mK showing the appearance of new peaks below the transition temperature. (d) Temperature dependence of the $(\frac{1}{2}, 0, \frac{1}{2})$ peak intensity. In (b) the grey line indicates the background intensity for the Q position of the $(\frac{1}{2}, 0, \frac{1}{2})$ peak determined from the 1.4 K diffraction pattern.

~0.2 K with a tail up to ~0.4 K, revealing a second-order phase transition in $KErSe_2$. The inset in Fig. 1 presents the temperature dependence of the entropy at 0 T. The released entropy is close to 3 J/mol K only at the transition and increases to the expected value $R \ln 2$ for Kramers doublets at ~2 K. This result is similar to that for the previously reported Ce/Yb compounds [33,37], indicating the possible short-range interaction by disorders or spin fluctuation, which is also hinted at by the neutron results below. When the magnetic fields were applied along the c axis, the long-range order was suppressed to low temperature and vanished at 0.5 T. Considering the dome shape in the H-T phase diagram in $NaYbO_2$, we believe this field dependence relation possibly indicates a magnetic structure different from the up-up-down structure in $NaYbO_2$ [32]. Additionally, a broad peak appears at ~0.15 K at 0.5 T and shifts to a higher temperature of ~0.4 K at 0.75 T. This broad peak could be explained by the possible ferromagnetic component and/or Schottky effect.

B. Neutron scattering

In order to investigate the nature of the long-range magnetic order, as indicated by the heat capacity measurements, neutron powder diffraction patterns were collected between 2 and 0.08 K. A representative pattern collected above the signal seen in the heat capacity (i.e., at 800 mK) is shown together with a best-fit model determined by Rietveld refinement [Fig. 2(a)]. As can be seen, the previously reported delafossite crystal structure with $R\bar{3}m$ space group symmetry adequately accounts for the observed peak positions and intensities [40,42]. Table I lists the crystallographic parameters for two selected temperatures obtained from Rietveld refinements.

Figure 2(c) shows neutron diffraction patterns collected at 1.4 K and 45 mK, which are above and below the feature temperature of the heat capacity result. As can be seen, at several positions new peaks arise in the 45 mK data, indicating symmetry breaking. Collecting the intensity of the peak at 0.89 $Å^{-1}$ as a function of temperature [Fig. 2(d)] reveals that the transition occurs at ~370 mK. Considering the probable thermal lagging during the order parameter scan, this transition temperature corresponds to the magnetic transition observed in the heat capacity measurements. Given the low scattering angle of these peaks, the low temperature of the transition, and the form factor, we assume these peaks have a magnetic origin rather than being due to a structural transition and endeavor to model them using the tools of representational analysis for the magnetic structure solution.

TABLE I. Crystallographic parameters of $KErSe_2$ at 370 and 45 mK. Parameters were determined from Rietveld refinements performed using NPD collected on the HB-2A diffractometer with the 2.41-Å incident wavelength. The atomic displacement parameters and magnetic moments are reported in units of $Å^{-1}$ and μ_B/Er, respectively. We note that the K and Er ions sit on the (0,0,0) 3*a* and $(0, 0, \frac{1}{2})$ 3*b* Wyckoff sites, respectively, and so have no refinable component to their atomic positions. Only Se has a refinable atomic position at the $(0, 0, z)$ 6*c* Wyckoff site. Atomic displacement parameters are not reported due to the optimization of the experiment for magnetic studies which precluded the high-Q data necessary for their reliable modeling.

T	370 mK	45 mK
Space group	$R\bar{3}m$	$R\bar{3}m$
R_{wp}	6.38%	6.06%
a (Å)	4.1455(2)	4.1453(1)
c (Å)	22.711(1)	22.710(1)
V ($Å^3$)	338.01(3)	337.96(2)
Er (3*b*)		
M		3.06(1)
Se (6*c*)		
z	0.2351(2)	0.2354(2)

The appearance of new reflections at Q positions distinct from the nuclear structure tells us that the magnetic order must have a nonzero ordering vector. We find that all of these additional peaks can be indexed by a $(\frac{1}{2}, 0, \frac{1}{2})$ k vector and report in Table II the decomposition of the $R\bar{3}m$ space group with the $(\frac{1}{2}, 0, \frac{1}{2})$ ordering vector for the 3*b* site. This analysis shows two irreducible representations Γ (corresponding to two magnetic space groups) are allowed, which together generate three possible basis vectors Ψ. Considering the structures, we find that Γ_1 allows moments only in the *a*-*b* plane along the *b* axis, while Γ_2 has an in-plane component rotated away from either *a* or *b* and also (via Ψ_3) allows for a moment component along the *c* axis. Representative magnetic structures for both irreducible representations are shown in Fig. 3.

To discriminate between the two models, Rietveld refinements were performed using the zero-field data and the magnetic structure generated by each irreducible representation. The resulting best-fit calculated diffraction patterns are shown together with the experimental data in Fig. 2(b). As seen, Γ_1 visually reproduces the experimental data better, despite having fewer refinable parameters, so we focus on that model for the zero-field structure.

TABLE II. Irreducible representations Γ, constituent basis vectors ψ, basis vector directions, and magnetic space groups for the $R\bar{3}m$ nuclear symmetry with $k = (\frac{1}{2}, 0, \frac{1}{2})$.

Γ	ψ	Components of ψ	Magnetic space group
Γ_1			C_C2/m
	ψ_1	$(0, -1, 0)$	
Γ_2			C_C2/c
	ψ_2	(2,1,0)	
	ψ_3	(0,0,2)	

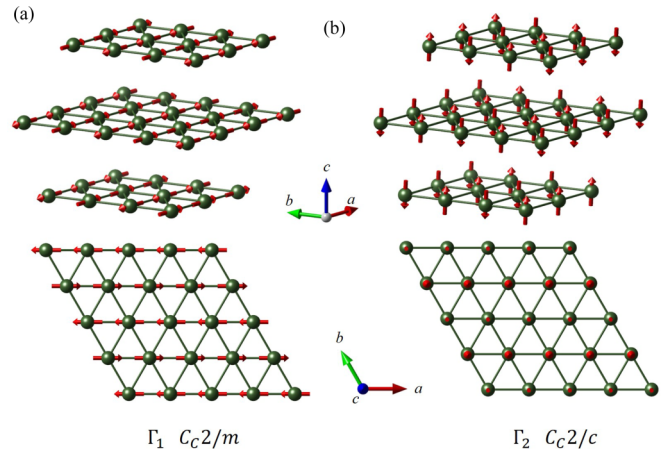

FIG. 3. Best-fit magnetic structures of the two irreducible representations formed from the decomposition of $R\bar{3}m$ with $k = (\frac{1}{2}, 0, \frac{1}{2})$. Along *c* only half of the doubled magnetic unit cell is visualized in the top two panels.

The fitted zero-field magnetic structure is shown in Fig. 3(a). As described, the symmetry of Γ_1 allows only a nonzero magnetic moment along the *b* axis. From our refinements, our extracted moment is $3.06(1)\mu_B$/Er. We note that this is significantly less than the $\sim 9.6\mu_B$/Er expected for the Er^{3+} ion and less than the effective moment reported previously from magnetic susceptibility and other Er^{3+} compounds with a similar valence [40,48]. There are several mechanisms which could cause this discrepancy: disorder leading to only partial ordering of the Er sites, strong frustration, and/or fluctuations preventing the full Er^{3+} moment from ordering or issues with thermometry and thermal conduction leading to a nonsaturated moment in our base temperature run. For the latter, as described previously, we endeavored to ensure thermalization at millikelvin temperatures, so we focus on the former two possibilities.

To discriminate among the fluctuation, frustration, and disorder scenarios using our diffraction data we note that short-range static or fluctuating correlations can be observed in neutron powder diffraction patterns as background features. This occurs because short-range static correlations can cause broad diffuse features and fluctuations may be integrated into the diffraction pattern due to the finite energy of the incident neutrons and the diffractometer's inability to discriminate for purely elastic scattering. Looking at the background in Fig. 2, we note that unlike the usually flat isotropic background observed on the HB-2A diffractometer [43], we see a generally "lumpy" nonlinear background in both the 800 and 45 mK scans. Such a signal may be indicative of diffuse scattering coming from the sample.

In order to identify any contribution to the background arising from magnetic scattering from the sample we look at difference curves between the sample under different field and temperature conditions, as shown in Fig. 4(a). Comparing first the 1.4 K and 45 mK data, we see a slight increase in the background at low Q in the 1.4 K run, as might be expected from the paramagnetic state for which increased low-Q scattering is expected from the bare form factor of the Er^{3+} ion (see, for instance, [48,49]). The lack of a significant feature here is

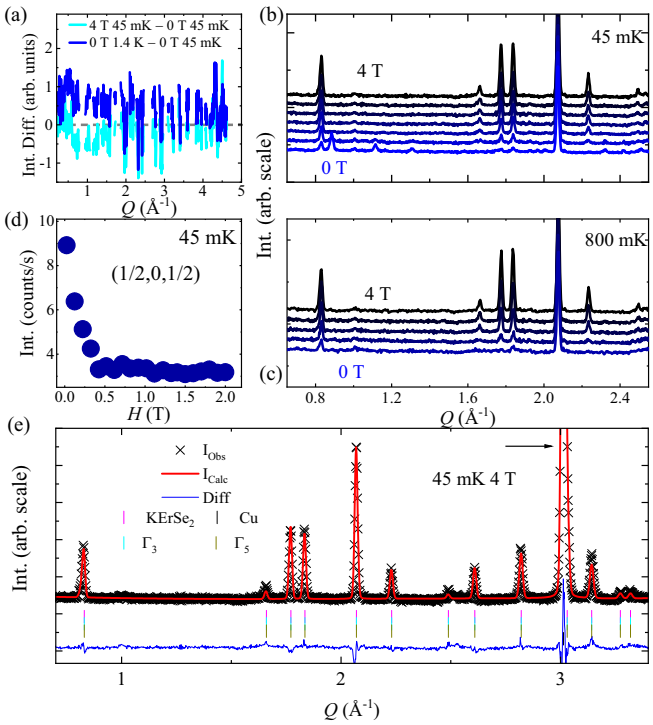

FIG. 4. (a) Difference curves of diffraction patterns collected at various temperatures and fields. Diffraction patterns collected under applied fields at (b) 45 and (c) 800 mK. (d) Order parameter scan on the $(\frac{1}{2}, 0, \frac{1}{2})$ magnetic Bragg reflection as a function of applied magnetic field collected at 45 mK. (e) Neutron powder diffraction data, together with best-fit models determined from Rietveld refinements for data collected at 45 mK under an applied field of 4 T. The data, model, difference, and phase peak indexes are indicated by black crosses, red lines, blue lines, and tick marks, respectively. The Cu peaks are also indicated by an arrow due to the overlapping difference curve.

consistent with the similarly lumpy background seen in both high- and low-temperature scans in Fig. 2, which indicates its source persists to 1.4 K.

As another test, we compare low-temperature patterns collected in 0- and 4-T applied fields [Fig. 4(a)]. In this difference curve a more significant change is apparent, and an obvious dip around 1 $Å^{-1}$ is seen. As will be discussed later, both scans are in a magnetically ordered state and at the same temperature; therefore, this change cannot be due to paramagnetic scattering from Er^{3+} ions. Instead, it is consistent with the applied field either polarizing static magnetically disordered regions into a ferromagnetic (FM) state or, similarly, pushing fluctuating spins into long-lived (FM) states which contribute to Bragg reflections rather than diffuse scattering [50]. Either of these explanations is consistent with the loss of diffuse intensity around 1 $Å^{-1}$ upon applying a magnetic field. We note that similar difference curves are seen for all applied fields; even the (45 mK, 0.25 T) and (45 mk, 0 T) difference curves exhibit a decreased low-q background relative to the zero-field difference curve.

From this observation we suggest it is likely that the reduced ordered moment for Er^{3+} obtained from our Rietveld analysis is due to either partial static disorder where portions

TABLE III. Irreducible representations Γ, constituent basis vectors ψ, basis vector directions, and magnetic space groups for the $R\bar{3}m$ nuclear symmetry with $k = (0, 0, 0)$.

Γ	ψ	Components of ψ	Magnetic space group
Γ_3			$R\bar{3}m'$
	ψ_1	(0,0,12)	
Γ_5			
	ψ_2	$(0, -3, 0)$	$C2/m$
	ψ_3	$(-3.5, -1.7, 0)$	$C2'/m'$

of the Er sublattice do not conform to the long-range magnetic order or part of the Er^{3+} spin remaining in a fluctuating state (see, for instance, work on $Er_2Ti_2O_7$ in [51–53]). While our current analysis is insufficient to discriminate between these scenarios decisively, we note that as only a small applied field is able to suppress the diffuse scattering, the fluctuation scenario may be more likely because a larger field would be expected to be necessary to polarize static magnetic disorder. For instance, with a Curie-Weiss temperature of $|\theta_{CW}| \sim 4$ K we can estimate an overall exchange constant of around 50 meV, considering that the smallest measured field of 0.25 T was adequate to reduce the diffuse background we can estimate an energy scale of ∼40 meV to polarize the disordered state. Though both of these values are rough estimates, they suggest that a larger field should be necessary to overcome exchange interactions. The reduced moment of Er^{3+} is corroborated, at least in part, by recent studies explicating the magnetic Hamiltonian which suggested the possibility of quantum fluctuations in the magnetic ground state [42]. However, additional studies on single crystals are needed to look for firmer evidence of diffuse scattering and its potential features in uncollapsed *HKL* space as well as measuring the spin waves in the ordered state.

Encouraged by our heat capacity results, we performed neutron powder diffraction measurements under applied magnetic fields to look for a change in the long-range magnetic order. Powder patterns collected at 45 and 800 mK under applied fields from 0 to 4 T are shown as waterfall plots in Figs. 4(b) and 4(c). At 45 mK, we observe the relatively quick suppression of the $(\frac{1}{2}, 0, \frac{1}{2})$-type magnetic state, with the associated magnetic Bragg peaks disappearing above 0.25 T. On the other hand, while peaks associated with the $(\frac{1}{2}, 0, \frac{1}{2})$ order are suppressed, a significant increase in intensity is seen on several low-Q nuclear Bragg peaks, which appears to saturate above 0.5 T, indicating the stabilization of a new magnetic order with $k = (0, 0, 0)$. Performing an order parameter scan as a function of applied field on the $(\frac{1}{2}, 0, \frac{1}{2})$ peak [Fig. 4(d)], we see its intensity is fully suppressed by 0.5 T. This suppression with the change in magnetic scattering to nuclear peak positions indicates a metamagnetic transition. This finding is consistent with the previous reported isothermal magnetization results [40].

Using $k = (0, 0, 0)$, we again perform a representational analysis to identify the possible magnetic structures under applied field, the results of which are shown in Table III. Again, only two Γ are found with a total of three Ψ. In this case the first irreducible representation (Γ_3) allows only a

moment along the c axis, while the second (Γ_5) has in-plane moments with one Ψ along b and the other rotated between the two in-plane lattice vectors.

Looking at the 800 mK waterfall plot [Fig. 4(c)], we find that even above the zero-field T_N the applied field is able to induce long-range magnetic order, in accord with the heat capacity measurements. As can be seen, the ($k = 0$)-type peaks, at positions where the nuclear intensities are otherwise weak, are clearly visible by 1 T. These peaks are identical in position and relative intensity to those of the low-temperature $k = 0$ magnetic structure described above, so we suggest they are an extension of that magnetic order to higher temperatures.

While it is generally suspect to attempt a magnetic structure solution for powder data in applied fields due to the lack of control over the field orientation with respect to the crystal lattice, considering the few possible structures consistent with $k = 0$, we attempt such an analysis nonetheless. In doing so we find that neither allowed Γ alone is able to produce an adequate fit to the data. However, if both Γ are used as two separate magnetic phases, we find we are able to reproduce the observed intensities quite well using only one Ψ from each Γ [Ψ_1 and Ψ_3; Fig. 4(e)]. The fitting result describes a state where the applied field pushes different grains of the powder sample into different magnetic structures ostensibly depending on their relative orientation with respect to the applied field (e.g., grains with the field mostly in plane may lead to one structure, while those with the field mostly out of plane may lead to another). As the $(\frac{1}{2}, 0, \frac{1}{2})$-type peaks are completely suppressed, we can surmise that the sample must be in one of three states: one of the two ($k = 0$)-type magnetic structures or a paramagnetic (PM) state. As refinements of the magnetic phases rely on intensities arising purely from the magnitude of the magnetic moment, it is not possible to uniquely determine phase fractions or magnetic moments for either structure or whether the entire sample is ordered or whether some of it has become PM. Such questions will require follow-up diffraction studies performed with applied fields on a single-crystal sample.

However, from our work we can say that an applied magnetic field drives a metamagnetic transition from the $(\frac{1}{2}, 0, \frac{1}{2})$-type order to a FM $k = 0$ state. Additionally, our analysis shows that one of two structures is adopted (likely depending on the field's orientation with respect to the crystal lattice), with one being a fully c polarized FM state [Fig. 5(a)] and the other being a FM structure with the moments in plane [Fig. 5(b)]. While the former may be more surprising due to the expected easy-plane-type single-ion physics in this material, the latter is less so and ostensibly indicates the weak interlayer correlations which may be suppressed with a 0.5-T field from the antiferromagnetic (AFM) interlayer correlations found in the 0-T structure to the currently discussed FM in-plane structure. As a final consideration, we revisit the field dependence of the heat capacity measurements in which this metamagnetic transition is less clear, lacking a sharp peaked signal. However, the neutron data clearly evidence a magnetic transition to an ordered state (most clearly via the order parameters identified by the two irreducible representations). Such an observation is inconsistent with a transition to a PM state, so we describe the ordered phase found under an applied field as FM.

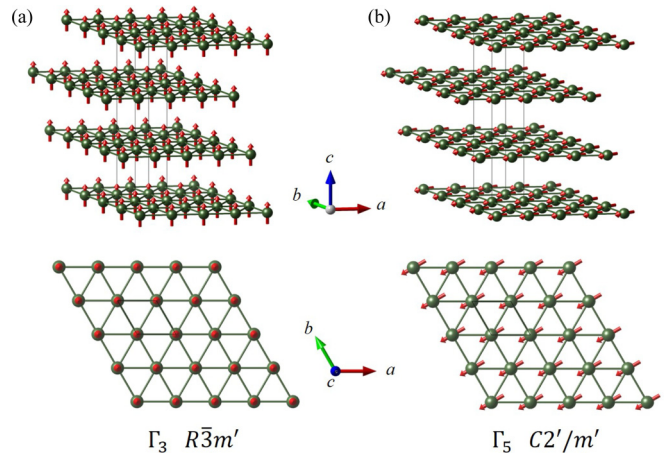

FIG. 5. Magnetic structures of the two irreducible representations formed from the decomposition of $R\bar{3}m$ with $k = (0, 0, 0)$.

C. Theory model

Anisotropic magnetic interactions could induce multiple magnetic ground states in the ideal triangular lattice. In a recent theoretical work, a nearest-neighbor spin-orbit-induced anisotropic-exchange Hamiltonian model was used and showed that the stripe order could be favored by the $J_\pm < 0$ term [54]. In addition, the transition temperature of the stripe order in $KErSe_2$ is much lower than the Curie temperature from magnetization. It indicates the stripe phase in $KErSe_2$ may be close to the transition boundaries from the anisotropic-exchange model. We observe a relatively small field drives the system to the ferromagnetic order experimentally.

We also want to induce the near-neighbor interaction model for the possible explanation of the strip magnetic order. From the crystal electronic field estimation, the easy-plane $KErSe_2$ could have a large component $Jz = 1/2$ term, which is able to give a relatively large moment and dipole-dipole interaction between Er ions. Based on the structure, we propose a simple two-dimensional Hamiltonian for $KErSe_2$:

$$\mathcal{H} = -\sum_{i,j} J_{ij} S_i S_j - K \sum_i {S_{ix}}^2, \tag{1}$$

where sites i and j on a triangular lattice are coupled by exchange J_{ij}. When the nearest-neighbor coupling J_1 is negative, this system is magnetically frustrated. However, this frustration can be lifted by second- and third-neighbor exchange couplings J_2 and J_3. All three exchange couplings are shown in Fig. 6(a).

The spin state observed in $KErSe_2$ has wave vector $\mathbf{Q} = (2\pi/a)(1, 0)$ in the xy plane. In terms of the reciprocal lattice vectors

$$\mathbf{b}_1 = \frac{2\pi}{a}(1, 1/\sqrt{3}), \tag{2}$$

$$\mathbf{b}_2 = \frac{2\pi}{a}(1, -1/\sqrt{3}), \tag{3}$$

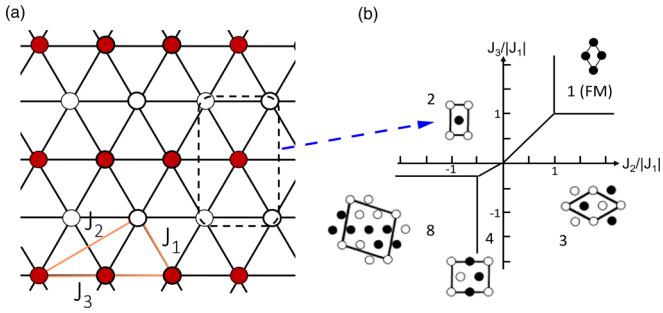

FIG. 6. (a) Triangular lattice with first-, second-, and third-neighbor couplings. The 2-SL magnetic unit cell is given by the dashed boundary. (b) Phase diagram of the triangular lattice showing the stable magnetic phases with interactions J_1, J_2, and J_3. Only collinear spin states are considered.

we can write $\mathbf{Q} = (1/2, 1/2) \equiv (\mathbf{b}_1 + \mathbf{b}_2)/2$. The spin state is sketched in Fig. 6(b), where dark circles mean the spin points to the right, and open circles mean the spin points to the left. This state has two spins in the magnetic unit cell, which is shown by the dashed boundary. In a previous study on the antiferromagnetic triangular lattice [55], the observed two-sublattice (2-SL) state could be stable over a wide range of $J_2/|J_1|$ and $J_3/|J_1|$, as shown in Fig. 6(b). $KErSe_2$ is a possible representative of this stripe spin state in the delafossite structure.

Previously, long-range magnetic order was found in Ce- and Yb-based delafossite materials, which contain the perfect rare-earth triangular lattice layers. The Ce-based compound $KCeS_2$ presents an antiferromagnetic order at zero field, while Yb-based materials present a spin liquid ground state and need an applied magnetic field to induce the long-range order [31–33,37]. The magnetic transitions present a dome shape in the H-T phase diagram in Ce and Yb compounds, which could be explained as the possible up-up-down magnetic structure in the triangular lattice. In $KErSe_2$ the magnetic transition monotonously decreases to lower temperature with increasing magnetic field. The significant difference between these results and the magnetic structure reveals possible multiple magnetic ground states in a similar magnetic triangular lattice with different rare-earth ions.

On the other hand, although the specific rare-earth ions play an important role in a similar delafossite structure, we could also tune the intralayer and interlayer distance by replacing the nonmagnetic ions and may find the boundaries of different spin states. Based on the experiments with Er- and Yb-based samples, the replacement of the nonmagnetic ions in rare-earth delafossites shows a slight influence on the magnetic properties [27,31,40]. In the phase diagram predicted by theory, multiple ground states could be explored by changing the strength of the interaction [54]. Our $KErSe_2$ result could help us to understand the phase diagram of the triangular lattice and discover the spin liquid state in rare-earth compounds.

IV. CONCLUSION

In conclusion, we used heat capacity and neutron powder diffraction to investigate the magnetism of $KErSe_2$ in the low-temperature region. The heat capacity revealed a long-range magnetic order at ∼0.2 K at zero field with a long tail up to ∼0.4 K. A magnetic field was found to suppress the magnetic transition to below 0.08 K at 0.5 T. Neutron powder diffraction results suggested the zero-field magnetic structure is an unusual stripe spin structure with a reduced moment of $3.06(1)\mu_B$/Er. Analysis of the powder patterns' "background" features revealed the presence of a magnetic diffuse signal even in the ordered state consistent with the observed reduced ordered moment. Diffraction data collected under an applied field confirmed the heat capacity results and indicated a metamagnetic transition from AFM to FM. Additionally, careful analysis showed that the metamagnetic transition is likely dependent on the direction of the applied field with respect to the crystal lattice, leading to at least two possible field-stabilized FM orders and a likely complex temperature/field magnetic phase diagram with several phases at similar energy scales. Using first-principles calculations we found that the anisotropic interactions or the two-dimensional Hamiltonian which considers the first-, second-, and third-neighbor couplings can explain this magnetic structure. Our results could help us to understand the phase diagram of rare-earth triangular lattice materials.

[1] J. F. Sadoc and R. Mosseri, *Geometrical Frustration*, Collection Alea-Saclay: Monographs and Texts in Statistical Physics (Cambridge University Press, Cambridge, 1999).

[2] R. Moessner and A. P. Ramirez, Geometrical frustration, Phys. Today **59**(2), 24 (2006).

[3] C. Lacroix, P. Mendels, and F. Mila, *Introduction to Frustrated Magnetism: Materials, Experiments, Theory*, Vol. 164 (Springer Science, New York, 2011).

[4] P. W. Anderson, Resonating valence bonds: A new kind of insulator? Mater. Res. Bull. **8**, 153 (1973).

[5] F. Mila, Quantum spin liquids, Eur. J. Phys. **21**, 499 (2000).

[6] L. Balents, Spin liquids in frustrated magnets, Nature (London) **464**, 199 (2010).

[7] Y. Li, H. Liao, Z. Zhang, S. Li, F. Jin, L. Ling, L. Zhang, Y. Zou, L. Pi, Z. Yang *et al.*, Gapless quantum spin liquid ground state in the two-dimensional spin-1/2 triangular antiferromagnet $YbMgGaO_4$, Sci. Rep. **5**, 16419 (2015).

[8] Y. Li, G. Chen, W. Tong, L. Pi, J. Liu, Z. Yang, X. Wang, and Q. Zhang, Rare-Earth Triangular Lattice Spin Liquid: A Single-Crystal Study of $YbMgGaO_4$, Phys. Rev. Lett. **115**, 167203 (2015).

[9] Y. Li, D. Adroja, P. K. Biswas, P. J. Baker, Q. Zhang, J. Liu, A. A. Tsirlin, P. Gegenwart, and Q. Zhang, Muon Spin Relaxation Evidence for the U(1) Quantum Spin-Liquid Ground State in the Triangular Antiferromagnet $YbMgGaO_4$, Phys. Rev. Lett. **117**, 097201 (2016).

[10] Y. Shen, Y.-D. Li, H. Wo, Y. Li, S. Shen, B. Pan, Q. Wang, H. C. Walker, P. Steffens, M. Boehm *et al.*, Evidence for a spinon Fermi surface in a triangular-lattice quantum-spin-liquid candidate, Nature (London) **540**, 559 (2016).

[11] J. A. M. Paddison, M. Daum, Z. Dun, G. Ehlers, Y. Liu, M. B. Stone, H. Zhou, and M. Mourigal, Continuous excitations of the triangular-lattice quantum spin liquid $YbMgGaO_4$, Nat. Phys. **13**, 117 (2017).

[12] X. Zhang, F. Mahmood, M. Daum, Z. Dun, J. A. M. Paddison, N. J. Laurita, T. Hong, H. Zhou, N. P. Armitage, and M. Mourigal, Hierarchy of Exchange Interactions in the Triangular-Lattice Spin Liquid $YbMgGaO_4$, Phys. Rev. X **8**, 031001 (2018).

[13] Y. Li, D. Adroja, R. I. Bewley, D. Voneshen, A. A. Tsirlin, P. Gegenwart, and Q. Zhang, Crystalline Electric-Field Randomness in the Triangular Lattice Spin-Liquid $YbMgGaO_4$, Phys. Rev. Lett. **118**, 107202 (2017).

[14] W. M. Steinhardt, Z. Shi, A. Samarakoon, S. Dissanayake, D. Graf, Y. Liu, W. Zhu, C. Marjerrison, C. D. Batista, and S. Haravifard, Constraining the parameter space of a quantum spin liquid candidate in applied field with iterative optimization, arXiv:1902.07825.

[15] Y. Shen, Y.-D. Li, H. C. Walker, P. Steffens, M. Boehm, X. Zhang, S. Shen, H. Wo, G. Chen, and J. Zhao, Fractionalized excitations in the partially magnetized spin liquid candidate $YbMgGaO_4$, Nat. Commun. **9**, 4138 (2018).

[16] Z. Zhu, P. A. Maksimov, S. R. White, and A. L. Chernyshev, Disorder-Induced Mimicry of a Spin Liquid in $YbMgGaO_4$, Phys. Rev. Lett. **119**, 157201 (2017).

[17] Z. Zhu, P. A. Maksimov, S. R. White, and A. L. Chernyshev, Topography of Spin Liquids on a Triangular Lattice, Phys. Rev. Lett. **120**, 207203 (2018).

[18] I. Kimchi, A. Nahum, and T. Senthil, Valence Bonds in Random Quantum Magnets: Theory and Application to $YbMgGaO_4$, Phys. Rev. X **8**, 031028 (2018).

[19] S. Mitsuda, H. Yoshizawa, N. Yaguchi, and M. Mekata, Neutron diffraction study of $CuFeO_2$, J. Phys. Soc. Jpn. **60**, 1885 (1991).

[20] J. P. Kemp, P. A. Cox, and J. W. Hodby, Magnetic susceptibility studies of $LiNiO_2$ and $NaNiO_2$, J. Phys.: Condens. Matter **2**, 6699 (1990).

[21] P. F. Borgers and U. Enz, Metamagnetism of $NaNiO_2$, Solid State Commun. **4**, 153 (1966).

[22] S. Komaba, C. Takei, T. Nakayama, A. Ogata, and N. Yabuuchi, Electrochemical intercalation activity of layered $NaCrO_2$ vs. $LiCrO_2$, Electrochem. Commun. **12**, 355 (2010).

[23] A. Olariu, P. Mendels, F. Bert, B. G. Ueland, P. Schiffer, R. F. Berger, and R. J. Cava, Unconventional Dynamics in Triangular Heisenberg Antiferromagnet $NaCrO_2$, Phys. Rev. Lett. **97**, 167203 (2006).

[24] M. Poienar, F. Damay, C. Martin, J. Robert, and S. Petit, Spin dynamics in the geometrically frustrated multiferroic $CuCrO_2$, Phys. Rev. B **81**, 104411 (2010).

[25] H. Kadowaki, H. Kikuchi, and Y. Ajiro, Neutron powder diffraction study of the two-dimensional triangular lattice antiferromagnet $CuCrO_2$, J. Phys.: Condens. Matter **2**, 4485 (1990).

[26] S. Mitsuda, N. Kasahara, T. Uno, and M. Mase, Partially disordered phase in frustrated triangular lattice antiferromagnet $CuFeO_2$, J. Phys. Soc. Jpn. **67**, 4026 (1998).

[27] J. Xing, L. D. Sanjeewa, J. Kim, G. R. Stewart, M.-H. Du, F. A. Reboredo, R. Custelcean, and A. S. Sefat, Crystal synthesis and frustrated magnetism in triangular lattice $CsRESe_2$ (RE = LaLu): Quantum spin liquid candidates $CsCeSe_2$ and $CsYbSe_2$ ACS Mater. Lett. **2**, 71 (2019).

[28] W. Liu, Z. Zhang, J. Ji, Y. Liu, J. Li, X. Wang, H. Lei, G. Chen, and Q. Zhang, Rare-earth chalcogenides: A large family of triangular lattice spin liquid candidates, Chin. Phys. Lett. **35**, 117501 (2018).

[29] M. Baenitz, Ph. Schlender, J. Sichelschmidt, Y. A. Onykiienko, Z. Zangeneh, K. M. Ranjith, R. Sarkar, L. Hozoi, H. C. Walker, J.-C. Orain, H. Yasuoka, J. van den Brink, H. H. Klauss, D. S. Inosov, and Th. Doert, $NaYbS_2$: A planar spin-1/2 triangular-lattice magnet and putative spin liquid, Phys. Rev. B **98**, 220409(R) (2018).

[30] L. Ding, P. Manuel, S. Bachus, F. Grußler, P. Gegenwart, J. Singleton, R. D. Johnson, H. C. Walker, D. T. Adroja, A. D. Hillier, and A. A. Tsirlin, Gapless spin-liquid state in the structurally disorder-free triangular antiferromagnet $NaYbO_2$, Phys. Rev. B **100**, 144432 (2019).

[31] K. M. Ranjith, D. Dmytriieva, S. Khim, J. Sichelschmidt, S. Luther, D. Ehlers, H. Yasuoka, J. Wosnitza, A. A. Tsirlin, H. Kühne, and M. Baenitz, Field-induced instability of the quantum spin liquid ground state in the $J_{\text{eff}} = \frac{1}{2}$ triangular-lattice compound $NaYbO_2$, Phys. Rev. B **99**, 180401(R) (2019).

[32] M. M. Bordelon, E. Kenney, C. Liu, T. Hogan, L. Posthuma, M. Kavand, Y. Lyu, M. Sherwin, N. P. Butch, C. Brown *et al.*, Field-tunable quantum disordered ground state in the triangular lattice antiferromagnet $NaYbO_2$ Nature Phys. **15**, 1058 (2019).

[33] J. Xing, L. D. Sanjeewa, J. Kim, G. R. Stewart, A. Podlesnyak, and A. S. Sefat, Field-induced magnetic transition and spin fluctuations in the quantum spin-liquid candidate $CsYbSe_2$, Phys. Rev. B **100**, 220407(R) (2019).

[34] K. M. Ranjith, S. Luther, T. Reimann, B. Schmidt, Ph. Schlender, J. Sichelschmidt, H. Yasuoka, A. M. Strydom, Y. Skourski, J. Wosnitza, H. Kühne, Th. Doert, and M. Baenitz, Anisotropic field-induced ordering in the triangular-lattice quantum spin liquid $NaYbSe_2$, Phys. Rev. B **100**, 224417 (2019).

[35] T. Ferreira, J. Xing, L. D. Sanjeewa, and A. S. Sefat, Frustrated magnetism in triangular lattice $TlYbS_2$ crystals grown via molten flux, Front. Chem. **8**, 127 (2020).

[36] P-L Dai, G. Zhang, Y. Xie, C. Duan, Y. Gao, Z. Zhu, E. Feng, C-L. Huang, H. Cao, A. Podlesnyak *et al.*, Spinon Fermi surface spin liquid in a triangular lattice antiferromagnet $NaYbSe_2$, arXiv:2004.06867.

[37] G. Bastien, B. Rubrecht, E. Haeussler, P. Schlender, Z. Zangeneh, S. Avdoshenko, R. Sarkar, A. Alfonsov, S. Luther, Y. A. Onykiienko, H. C. Walker, H. Kuhne, V. Grinenko, Z. Guguchia, V. Kataev, H. H. Klauss, L. Hozoi, J. van den Brink, D. S. Inosov, B. Buchner, A. U. B. Wolter, and T. Doert, Long-range magnetic order in the s = 1/2 triangular lattice antiferromagnet $KCeS_2$, SciPost Phys. **9**, 041 (2020).

[38] Y. Cai, C. Lygouras, G. Thomas, M. N. Wilson, J. Beare, S. Sharma, C. A. Marjerrison, D. R. Yahne, K. A. Ross, Z. Gong, Y. J. Uemura, H. A. Dabkowska, and G. M. Luke, μSR study of the triangular Ising antiferromagnet $ErMgGaO_4$, Phys. Rev. B **101**, 094432 (2020).

[39] F. A. Cevallos, K. Stolze, and R. J. Cava, Structural disorder and elementary magnetic properties of triangular lattice $ErMgGaO_4$ single crystals, Solid State Commun. **276**, 5 (2018).

[40] J. Xing, L. D. Sanjeewa, J. Kim, W. R. Meier, A. F. May, Q. Zheng, R. Custelcean, G. R. Stewart, and A. S. Sefat,

Synthesis, magnetization, and heat capacity of triangular lattice materials $NaErSe_2$ and $KErSe_2$, Phys. Rev. Mater. **3**, 114413 (2019).

[41] S. Gao, F. Xiao, K. Kamazawa, K. Ikeuchi, D. Biner, K. W. Krämer, C. Rüegg, and T.-H. Arima, Crystal electric field excitations in the quantum spin liquid candidate $NaErS_2$, Phys. Rev. B **102**, 024424 (2020).

[42] A. Scheie, V. O. Garlea, L. D. Sanjeewa, J. Xing, and A. S. Sefat, Crystal-field Hamiltonian and anisotropy in $KErSe_2$ and $CsErSe_2$, Phys. Rev. B **101**, 144432 (2020).

[43] S. Calder, K. An, R. Boehler, C. R. Dela Cruz, M. D. Frontzek, M. Guthrie, B. Haberl, A. Huq, S. A. J. Kimber, J. Liu *et al.*, A suite-level review of the neutron powder diffraction instruments at Oak Ridge National Laboratory, Rev. Sci. Instrum. **89**, 092701 (2018).

[44] J. Rodríguez-Carvajal, Recent advances in magnetic structure determination by neutron powder diffraction, Phys. B (Amsterdam, Neth.) **192**, 55 (1993).

[45] L. W. Finger, D. E. Cox, and A. P. Jephcoat, A correction for powder diffraction peak asymmetry due to axial divergence, J. Appl. Crystallogr. **27**, 892 (1994).

[46] A. S Wills, A new protocol for the determination of magnetic structures using simulated annealing and representational analysis (SARAh), Phys. B (Amsterdam, Neth.) **276–278**, 680 (2000).

[47] K. Momma and F. Izumi, VESTA 3 for three dimensional visualization of crystal, volumetric and morphology data, J. Appl. Crystallogr. **44**, 1272 (2011).

[48] K. M. Taddei, L. Sanjeewa, J. W. Kolis, A. S. Sefat, C. de la Cruz, and D. M. Pajerowski, Local-Ising-type magnetic order and metamagnetism in the rare-earth pyrogermanate $Er_2Ge_2O_7$, Phys. Rev. Mater. **3**, 014405 (2019).

[49] D. M. Pajerowski, K. M. Taddei, L. D. Sanjeewa, A. T. Savici, M. B. Stone, and J. W. Kolis, Quantification of local Ising magnetism in rare-earth pyrogermanates $Er_2Ge_2O_7$ and $Yb_2Ge_2O_7$, Phys. Rev. B **101**, 014420 (2020).

[50] L. D. Sanjeewa, V. O. Garlea, M. A. McGuire, C. D. McMillen, and J. W. Kolis, Magnetic ground state crossover in a series of glaserite systems with triangular magnetic lattices, Inorg. Chem. **58**, 2813 (2019).

[51] K. A. Ross, Y. Qiu, J. R. D. Copley, H. A. Dabkowska, and B. D. Gaulin, Order by Disorder Spin Wave Gap in the *XY* Pyrochlore Magnet $Er_2Ti_2O_7$, Phys. Rev. Lett. **112**, 057201 (2014).

[52] J. P. C. Ruff, J. P. Clancy, A. Bourque, M. A. White, M. Ramazanoglu, J. S. Gardner, Y. Qiu, J. R. D. Copley, M. B. Johnson, H. A. Dabkowska, and B. D. Gaulin, Spin Waves and Quantum Criticality in the Frustrated *XY* Pyrochlore Antiferromagnet $Er_2Ti_2O_7$, Phys. Rev. Lett. **101**, 147205 (2008).

[53] P. D. de Réotier, A. Yaouanc, Y. Chapuis, S. H. Curnoe, B. Grenier, E. Ressouche, C. Marin, J. Lago, C. Baines, and S. R. Giblin, Magnetic order, magnetic correlations, and spin dynamics in the pyrochlore antiferromagnet $Er_2Ti_2O_7$, Phys. Rev. B **86**, 104424 (2012).

[54] P. A. Maksimov, Z. Zhu, S. R. White, and A. L. Chernyshev, Anisotropic-Exchange Magnets on a Triangular Lattice: Spin Waves, Accidental Degeneracies, and Dual Spin Liquids, Phys. Rev. X **9**, 021017 (2019).

[55] T. Takagi and M. Mekata, New partially disordered phases with commensurate spin density wave in frustrated triangular lattice, J. Phys. Soc. Jpn. **64**, 4609 (1995).